

Short-wave admittance correction for a time-domain cochlear transmission line model

François Deloche ^{*1}, Morgan Thienpont¹, and Sarah Verhulst¹

¹Hearing Technology @ WAVES, Department of Information Technology, Ghent University, Ghent, Belgium

February, 2026

Abstract

Transmission line (TL) models implemented in the time domain can efficiently simulate basilar-membrane (BM) displacement in response to transient or non-stationary sounds. By design, a TL model is well-suited for an one-dimensional (1-D) characterization of the traveling wave, but the real configuration of the cochlea also introduces higher-dimensional effects. Such effects include the focusing of the pressure around the BM and transverse viscous damping, both of which are magnified in the short-wave region. The two effects depend on the wavelength and are more readily expressed in the frequency domain. In this paper, we introduce a numerical correction for the BM admittance to account for 2-D effects in the time domain using autoregressive filtering and regression techniques. The correction was required for the implementation of a TL model tailored to the gerbil cochlear physiology. The model, which includes instantaneous nonlinearities in the form of variable damping, initially presented insufficient compression with increasing sound levels. This limitation was explained by the strong coupling between gain and frequency selectivity assumed in the 1-D nonlinear TL model, whereas cochlear frequency selectivity shows only a moderate dependence on sound level in small mammals. The correction factor was implemented in the gerbil model and made level-dependent using a feedback loop. The updated model achieved some decoupling between frequency selectivity and gain, providing 5 dB of additional gain and extending the range of sound levels of the compressive regime by 10 dB. We discuss the relevance of this work through two key features: the integration of both analytical and regression methods for characterizing BM admittance, and the combination of instantaneous and non-instantaneous nonlinearities.

I Introduction

Cochlear macromechanics, simplified to a single degree of freedom such as basilar membrane (BM) displacement, can be described by a transmission line (TL) model capturing the essential features of the cochlear traveling wave. When incorporated into a pipeline that reproduces the various stages of the auditory pathway (i.e., inner hair cells, auditory synapse and nerve, brainstem nuclei) (Verhulst et al. 2018), TL models can compete with more phenomenological models to generate evoked responses associated with the auditory periphery (Saremi et al. 2016; Vecchi et al. 2022). Specific strengths of the TL model include the simulation of otoacoustic emissions and the reproduction of instantaneous nonlinearities. Simulations in the time domain require a fine spatio-temporal sampling, but computations can be accelerated through efficient numerical schemes (Altoè et al. 2014) or, most effectively, by training a deep neural network to reproduce the mapping between sound input and BM output (Baby et al. 2021).

TL models effectively capture the traveling wave that propagates along the BM in response to sounds, but their unidimensional (1-D) nature can complicate the integration of effects that span multiple dimensions. Some of these effects can be implicitly integrated into the 1-D characterization of the traveling wave. For example, the property of ‘scaling symmetry’, which expresses the BM admittance as a function of normalized

^{*}e-mail: francois.delocne@polytechnique.org

frequency, has a formal connection with the tapering geometry of the cochlea (Shera and Zweig 1991). This property ensures that the driving pressure travels with a constant amplitude before reaching its peak, akin to a planar wave (Altoè and Shera 2020). Another aspect to consider is the stability of the TL model, since the active cochlea has regions of negative damping basal to each characteristic place that make cochlear models prone to instability. In 2-D or 3-D models, stability can be maintained by adding a viscous term dependent on the transverse gradient of fluid velocity (Sisto et al. 2021, 2023). As the wave approaches the peak region, this viscous term increases in magnitude relative to BM velocity: the damping of the wave grows rapidly, naturally restraining the region of negative damping. The case is more complicated for time-domain TL models. An ingenuous workaround proposed by Zweig (Zweig 1991) and further developed by Shera (Shera 2001) involves adding a slow-acting, time-delayed stiffness to the BM to restrain the region of negative damping to a region basal to the characteristic place. This solution was integrated into a comprehensive computational framework of the auditory periphery (Verhulst et al. 2012, 2015, 2018). The corresponding TL model, referred to as the V-1D model, serves as the basis for the model presented in this paper.

Although the BM admittance in the V-1D model includes a slow feedback term, it remains based on a modified harmonic oscillator. As a result, gain is tightly coupled to frequency selectivity, similar to a classical second-order filter: a narrowly tuned BM admittance produces frequency responses with a tall peak, while broader frequency responses are associated with lower gain. This property is not a critical issue for simulating human auditory responses because cochlear filters in humans are believed to be significantly sharper than those of small mammals (Shera et al.; Verschooten et al. 2018; Serra and Charaziak 2019). This sharper tuning aligns well with the broad range of compression of the cochlear response. The problem is more apparent for models reproducing the auditory responses of common laboratory animals, which are of particular interest because they can be tested against a wider range of physiological data that require invasive techniques. For many of these animals (e.g., gerbils), at low sound levels where the cochlea is in its most sensitive state, the peak of the BM velocity frequency response is tall but relatively broad (Fallah et al. 2021; He et al. 2022). Looking at multiple sound levels, the range of compression is large, but the broadening of tuning is quite limited. This apparent discrepancy posed a challenge during recent efforts to adapt the V-1D model to small rodents, specifically gerbils and mice (Thienpont et al. 2024). In our initial attempt to match cochlear responses in the gerbil, the model lacked approximately 10 dB of compression to achieve the desired variation in response gain.

In 2-D or 3-D models of the cochlea, part of the magnitude of the wave peak can be attributed to the phenomenon of pressure focusing occurring in the short-wave region. This effect is due to the decrease in the characteristic height of the pressure field associated with the shortening of the wavelength (Reichenbach and Hudspeth 2014). As the characteristic height is reduced when approaching the wave peak, the pressure becomes ‘focused’ in a thin layer around the basilar membrane. This translates into a positive gain factor on the pressure driving BM velocity. This phenomenon is passive, but if cochlear compressive nonlinearities are associated with an increase in wavelength, it has a stronger effect in the most active state (Sisto et al. 2021). In this case, pressure focusing extends the range of the cochlear response gain while having a limited impact on frequency selectivity.

In this paper, we use several numerical methods to simulate gain compensation from pressure focusing in a TL model tailored to the gerbil physiology. The correction is based on the work by Sisto et al. that integrates 2-D dimensional fluid effects (viscous damping and pressure focusing) into a frequency-domain TL model (Sisto et al. 2021). We implement this correction in the time domain using autoregressive filtering and regression methods. Beyond the task-specific improvements presented here, the new method may prove useful in various scenarios where wavelength-dependent effects need to be accounted for in a TL model, a challenge for time-domain implementations.

II Methods

In the Methods section, we use the following naming convention to refer to the two transmission line (TL) models which we aim to combine in this work:

- The **V-1D model** refers to the time-domain TL implementation described in Verhulst et al. (Verhulst

et al. 2018), which builds upon Zweig and Shera’s characterization of the BM admittance (Zweig 1991; Shera 2001).

- The **S-2D model** designates the frequency-domain WKB approximation of the pressure wave proposed by Sisto et al (Sisto et al. 2021). The model incorporates two 2-D hydrodynamic effects: pressure focusing and viscous damping, and serves as a reference for the short-wave admittance correction introduced in this paper.

Our contribution is the proposal of a third TL model, the **V^* model**, which is largely based on the framework of the V-1D model, but incorporates some elements from the S-2D model.

The Methods section is divided into two parts. The first three subsections review key elements of the V-1D and S-2D models to establish a common framework for the V^* model. The last subsection describes the implementation of the short-wave admittance correction.

II.1 Short-wave gain enhancement from pressure focusing (S-2D model)

We begin with the presentation of the S-2D model, as it clarifies the connection between the TL equations and a 2-D physical model of the cochlear traveling wave. The equations integrate pressure focusing and fluid viscous stress acting on the BM. More details can be found in the original paper (Sisto et al. 2021).

In the S-2D model, the upper and lower cochlear ducts are viewed as two 2-D rectangular boxes of height H separated by the BM. The coordinates x and z correspond to the longitudinal and transverse directions, respectively. We define $p_d = p(z) - p(-z)$ as the pressure difference between the scalae above the BM and the scala tympani. $U = \int_0^H u_x dz$ is the volume velocity in the upper scalae, and \bar{p}_d is the differential pressure averaged along the transverse direction.

The “TL-like” equations characterizing the pressure wave are :

$$\frac{\partial \bar{p}_d}{\partial x} = -Z_f U \quad (1a)$$

$$\frac{\partial U}{\partial x} = v_{BM} = Y_{BM} p_d(z = 0^+), \quad (1b)$$

where $Z_f = \frac{2j\omega\rho}{H}$, and Y_{BM} is the BM admittance relating BM velocity to the pressure difference applied across it.

The equations are almost reduced to a one-dimensional case, but in Eq. 1a, the pressure \bar{p}_d represents an average along the transverse direction, whereas in Eq. 1b, p_d is evaluated at $z = 0^+$ which corresponds to the BM upper surface. By introducing $\alpha = p_d(z = 0^+)/\bar{p}_d$, the ‘pressure focusing’ factor, the second equation can be rewritten as:

$$\frac{\partial U}{\partial x} = Y_{BM} \alpha \bar{p}_d. \quad (2)$$

Assuming that $Y_{BM} \alpha$ is a known function of the position x and the pulsation ω , the 1-D formalism can be used. By combining Equations 1a and 2, we obtain the wave equation:

$$\frac{\partial^2 \bar{p}_d}{\partial x^2} = -\kappa^2 \bar{p}_d, \quad (3)$$

with $\kappa^2 = Z_f Y_{BM} \alpha$.

By applying the WKB approximation to a 2-D box model, we obtain the following formula for the pressure focusing factor:

$$\alpha = \frac{\kappa H}{\tanh \kappa H} , \quad (4)$$

leading to the dispersion relation (Reichenbach and Hudspeth 2014):

$$\kappa \tanh(\kappa H) = 2j\rho\omega Y_{BM} . \quad (5)$$

In Sisto et al., this approach is extended to include the effect of fluid viscous stress acting on the BM. The viscous stress is proportional to the transverse gradient of (transverse) fluid velocity at $z = 0$. In the classical potential flow description, the latter is related to the second derivative of the pressure along z , whereas v_{BM} is related to the first derivative. The WKB approximation gives α/H for the ratio of the second to the first derivative. The viscous stress acting on the BM, derived in detail in Sisto et al., is therefore:

$$S = -4b\mu \frac{\alpha}{H} v_{BM} , \quad (6)$$

where μ is the dynamic viscosity of the fluid and $b = 2.5$ is an empirical factor to take into account the irrational part of the fluid flow (Sisto et al. 2021)¹. The BM admittance is derived from a harmonic oscillator model, updated to include the viscous stress:

$$Y_{BM} = -\frac{j\omega}{\sigma_{BM}} \left[-\omega^2 + j\omega \left(\Gamma + \frac{4\alpha b \mu}{\sigma_{BM} H} \right) + \omega_{bm}^2 \right]^{-1} . \quad (7)$$

In this formula, ω_{BM} is the characteristic frequency of the BM, and σ_{BM} is the effective mass density of the BM. Γ is a standard damping term, which can be further decomposed into active and passive components: $\Gamma = \Gamma_a + \Gamma_p$ with $\Gamma_p = \omega_{BM}$ and $\Gamma_a = -G\omega_{BM}$. The variable G represents the strength of the active process, which contributes to negative damping.

The updated BM admittance leads to the dispersion relation:

$$\kappa \tanh(\kappa H) = \frac{2\omega^2 \rho}{\sigma_{BM}} \left[\omega_{bm}^2 - \omega^2 + j\omega \left(\Gamma + \frac{4\alpha b \mu}{\sigma_{BM} H} \right) \right]^{-1} . \quad (8)$$

This relation introduces an additional layer of complexity to the case where Y_{BM} is independent of κ , as the factor α , which depends on κ , appears on the right-hand side of the equation. To compute κ , the recursive procedure described in Sisto et al. is used. After convergence, the pressure focusing factor α is calculated using Eq. 4. For the purpose of this paper, we also introduce the β factor, which captures the variations of α relative to a reference value:

$$\beta = \alpha/\alpha_0 , \quad (9)$$

where α_0 is the pressure focusing factor computed at a reference level. The S-2D parameters used in our calculations were essentially the same as in Sisto et al. (reported in Table 1), but we adapted the value of H to reflect the height of the gerbil cochlea at the mid-point between the base and apex ($CF = 4$ kHz).

II.2 Time-domain implementation: baseline (V-1D model)

Before presenting the strategy for integrating the pressure focusing factor, we review some elements of the V-1D TL model that serves as the basis for the time-domain implementation. The V-1D model consists of $N = 1000$ cascaded sections representing N segments of the cochlear partition from the base to the apex.

¹Note that the empirical factor $b = 2.5$ was not included in a more recent work (Sisto et al. 2023); here, we kept this factor to maintain consistency with the 2021 paper.

Each section includes a series impedance Z_{s_n} and a shunt (parallel) admittance Y_{p_n} (Zweig 1991; Verhulst et al. 2012, 2018) :

$$Z_{s_n}(j\omega) = M_{s_n} j\omega , \quad (10)$$

$$Y_{p_n}(j\omega) = \frac{j\omega}{M_{p_n}} \left[\omega_n^2 - \omega^2 + \delta_n j\omega \omega_n - \varrho_n e^{-j\psi_n \omega/\omega_n} \omega_n^2 \right]^{-1} . \quad (11)$$

n indexes the TL sections from 0 (base) to $N - 1$ (apex). The mass parameters scale as for a tapered guide with stiffness proportional to the characteristic frequency (Zweig 1991; Shera and Zweig 1991; Altoè and Shera 2020) : $M_{s_n} = \frac{\omega_0}{\omega_n} M_{s_0}$, and $M_{p_n} = \frac{\omega_0}{\omega_n} M_{p_0}$. The model is treated as a system of coupled differential equations solved numerically using Runge-Kutta (RK) 4(5), a finite-difference method. $\varrho_n e^{-j\psi_n \omega/\omega_n} \omega_n^2$ corresponds to a slow feedback term, with stiffness ϱ_n and delay ψ_n , integrated into the RK4(5) scheme using a spline interpolation (Altoè et al. 2014).

The V-1D model includes instantaneous nonlinearities that depend on the magnitude of the BM velocity. Specifically, the triplet $(\varrho_n, \delta_n, \psi_n)$ is updated over time to modify BM damping while ensuring that the corresponding (double) pole trajectory remains consistent with the near-invariance of BM velocity zero-crossings (Shera 2001). The formulas for determining the three parameters as a function of BM velocity can be found in previous work (Verhulst et al. 2018). The distance of the double pole from the imaginary axis in the s-domain determines the damping of the local BM impulse response. It is minimal at low sound levels and gradually increases to a saturating value across a range of sound levels where the response is compressive (Verhulst et al. 2018). This behavior mimics the level-dependent nature of cochlear tuning and response gain. Eventually, nonlinearities in the model are only determined by an initial state and a parameter a controlling the compression of the response (in dB/dB) as sound level increases. The initial state reflects the cochlea at low sound levels, where the BM response is most sharply tuned and exhibits the highest sensitivity (Ruggero et al. 1997). For animal models, the compression parameter can be derived from BM-velocity growth functions as the slope of the growth function represented on a logarithmic scale (Thienpont et al. 2024) .

The model version used in this study was calibrated to the gerbil physiology (parameters in Table 1). It is the same as the gerbil model described in Thienpont et al. (2024), but the frequency selectivity parameters were changed to reflect BM tuning rather than auditory nerve tuning. We made this choice to facilitate comparison of our model with BM vibration data. The poles in the V-1D model are set according to a power law relating the quality factor Q_{ERB} to center frequency (Verhulst et al. 2018). In Thienpont et al. (2024), this power law was matched to auditory nerve data (Müller 1996). In the present study, we used the same power law except that Q_{ERB} was divided by 1.9 to reflect BM tuning. This factor corresponds to the quality factor ratio between auditory-nerve and BM tuning reported in a recent study on cochlear frequency selectivity in the gerbil (Charaziak and Shera 2021).

II.3 Connections between the two TL models

So far, we have introduced two existing TL models (V-1D and S-2D). At this stage of the Methods section, it is useful to highlight their similarities and differences, and to emphasize that each serves a distinct purpose in the rest of the paper. Both models aim to characterize the cochlear traveling wave and its nonlinear behavior with sound level. They are based on coupled equations of pressure and velocity, which have been presented in the form of partial differential equations for the S-2D model (Eqs. 1a to 2), and in the form of a system of impedances for the V-1D model (Eqs. 10 and 11). One can therefore note many formal similarities between the two model, although different notations were used to avoid confusion between their respective parameters.

The two models, however, differ in several ways. The S-2D model is based on physical principles. This model is easier to solve numerically in the frequency domain, but the BM impedance does not have a closed-form expression, even in the frequency domain. By contrast, the V-1D model was specifically designed to provide

a relatively simple expression for the BM admittance and to reproduce time-domain characteristics such as the invariance of zero-crossings (Shera 2001). It is therefore more natural to consider the V-1D model as the basis of the time-domain implementation. The slow-delay feedback term in the admittance of V-1D model is not connected to any known physiological mechanism in the cochlea, but provides the necessary frequency modulation to alternate between negative and positive resistance regions in the frequency domain, ensuring numerical stability.

The two models also differ in their behavior when simulating traveling-wave responses, particularly in how the region of the wave peak is represented. In the V-1D model, the peak occurs at the transition between the stiffness- and mass-dominated regions, while in the S-2D model, the peak occurs at a more basal place (i.e., in the stiffness-dominated region). This difference will be stressed further in the Discussion section. Here, we simply note that it leads to different interpretations of the local BM resonant frequency in each model. In the V-1D model, the peak of the traveling wave in response to a tone coincides with the region of characteristic pulsation $\omega_n = 2\pi f$. In other words, at low sound levels the characteristic frequency CF and the best frequency BF are identical (Shera 2001). In the S-2D model, the wave is slowed down and peaks before it reaches its the characteristic place defined by the ratio of mass and stiffness (Sisto et al. 2021; Sisto and Moleti 2024), so that we have $BF < CF$ at the location of the peak. In practice, this discrepancy is resolved by applying an empirical affine relation to ω_{BM} so that the best frequencies of each model coincide. Based on WKB simulations of the S-2D model, we determined that $\omega_{BM} = 1.2\omega_n + 1500$ Hz, where ω_{BM} is the characteristic pulsation of the S-2D model, and the best frequency is equal to $\omega_n/(2\pi)$. This relationship is used to assign a value of ω_{BM} to each TL section for the calculation of the pressure focusing gain. The place-frequency mapping is set as in the V-1D model by a Greenwood function:

$$\omega_n = 2\pi A_1 (10^{-A_2 x} - B), \quad (12)$$

where x is the distance from base (in meter). The S-2D model is only used for computing the pressure focusing factor, which is a local property, so that we do not need to set a tonotopic mapping for S-2D to implement the methods described in the following subsections.

II.4 Implementation of the admittance correction (V^* model)

Figures 1 and 2 list the major steps of the implementation, divided into setup phase and runtime.

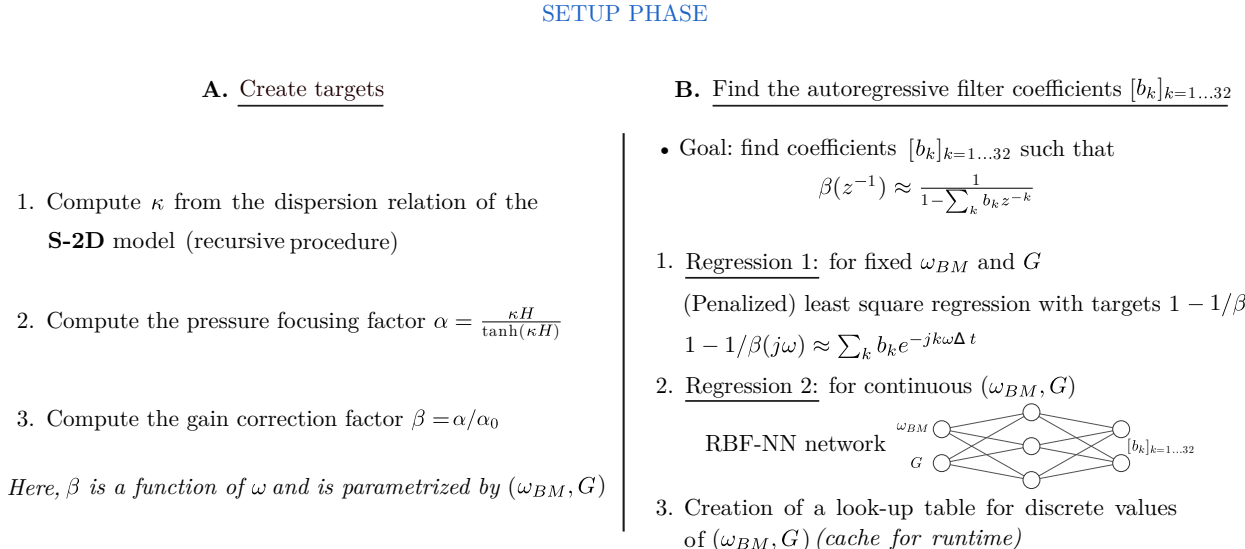


Figure 1: Implementation strategy for the setup of the admittance correction.

The general strategy is as follows:

A. Integration in the BM admittance

Adapted from Diependaal et al.

/ Altoë et al. (**V-1D** model)

1. Compute:

$$Q_n(t) = \sum_{k=1}^{32} b_{n,k} (\dot{v}_n[t - k\Delta t] + g_n[t - k\Delta t])$$

2. Solve $\mathbf{A} \mathbf{q} = \mathbf{g} - \mathbf{Q}$ 3. Compute $\dot{v}_n[t] = q_n[t] - g_n[t] + Q_n[t]$.**B. Update of the coefficients $[b_{n,k}]_{k=1 \dots 32}$:**1. Compute $\langle I_n \rangle$ (output intensity) with a 1st-order filter

2. Find G_n using a linear interpolation between G_{min} and G_{max} depending on $\langle I_n \rangle$ in dB3. Update $[b_{n,k}]_{k=1 \dots 32}$ for the section n with:

$$(\omega_{BM}, G) = (1.2 \omega_n + 1500, G_n)$$

Figure 2: Implementation strategy at runtime (when running simulations).

1. Create a function $\beta = \beta(\omega_{BM}, G)$ that returns the correction factor to apply to the BM admittance, computed from the S-2D model. The inputs of this function are the BM characteristic frequency and the strength of the ‘active process’. The output is a vector defined in the frequency domain.
2. Determine autoregressive coefficients to approximate β as the frequency response of an all-pole filter. The filter coefficients are denoted by $[b_k]_{k=1 \dots 32}$, and also depend on ω_{BM} and G . This step includes two regression methods that are run consecutively.
3. Update the time-domain equations to apply the recursive filters β , defined by the coefficients $[b_{n,k}]_{k=1 \dots 32}$, on top of the V-1D BM admittance.
4. During simulation: update the parameters $[b_{n,k}]_{k=1 \dots 32}$ over time to reflect changes in the active process, whose strength varies with the response intensity.

Steps 1 and 2 (setup phase) only needs to be run once to find the regression parameters defining the recursive filters. Steps 3 and 4 are executed when running the simulations. The following subsections describe each step in detail.

II.4.1 Estimation of the autoregressive filter coefficients

Our goal is to implement the gain missing in the V-1D model by introducing the pressure focusing factor α computed from the S-2D model (Eq. 4). However, since α can take large values that are difficult to incorporate directly in a time-domain implementation, we instead use the normalized β factor, introduced previously (Eq. 9: $\beta = \alpha/\alpha_0$). α_0 is the pressure focusing factor computed using the reference value $G = G_{REF}$ for the strength of the active process. G_{REF} is chosen as the midpoint of the range of values for G ($[G_{min}, G_{max}]$), to keep β as close as possible to 1. For clarity, we omit the full dependencies of β , which should be written as $\beta(\omega_{BM}, G, \omega)$. We call β a gain enhancement or correction factor, although in practice it can have a magnitude lower than 1. Note also that β has complex outputs, i.e., β is defined by its magnitude but also phase.

For a given pair (ω_{BM}, G) , we approximate β as the frequency response of an all-pole filter. Specifically, we want to find coefficients $[b_k]_{k=1 \dots 32}$ such that:

$$\beta(z^{-1}) \approx \frac{1}{1 - \sum_{k=1}^{32} b_k z^{-k}}. \quad (13)$$

We used 32 coefficients as a trade-off between accuracy and computational cost, but the method is general and can work with another number of coefficients. In the frequency domain, we can also write

$$1 - 1/\beta(j\omega) \approx \sum_{k=1}^{32} b_k e^{-jk\omega\Delta t}. \quad (14)$$

Table 1: Model and regression parameters. **Top:** Parameters for the S-2D model are the same as in (Sisto et al. 2021) (WKB simulations with $\mu = 10\mu_w$), except for the parameters in bold. **Middle:** Main parameters for the V-1D and V^* models. For more details on the model parametrization, refer to Thienpont et al. (2024).

S-2D model (calculation of α and β)	
H	320 μm
σ_{BM}	0.06 kg/m^2
ρ	$1.0 \times 10^3 \text{ kg}/\text{m}^3$
$\mu = 10\mu_w$	7.0 mPa s
$[\mathbf{G}_{\min}, \mathbf{G}_{\max}]$	[0, 1.3]
\mathbf{G}_{REF}	0.7
V-1D / V^* model (time-domain implementation)	
f_s (sampling frequency)	200 kHz
N (number of sections)	1000
H	320 μm
L (cochlear length)	12.1 mm
Greenwood A_1	50 216 Hz
Greenwood A_2	181.034 m^{-1}
Greenwood B	140 Hz
Q_{ERB} ($f_0 = 1$ kHz)	$1.45 \cdot (f/f_0)^{0.58}$
a (compression slope)	0.45 dB/dB
Regressions	
λ_1 (first LSE regression penalty)	1
λ_2 (second LSE regression penalty)	0.3
RBF-NN parameters	in text.

We use this formula to find the coefficients b_k . We discretize the equality over regularly spaced frequencies, representing each side as a vector in the frequency domain. We then determine the coefficients b_k that minimize the least-squares error (LSE) between these two vectors. We limit the computation of the LSE to frequencies up to $\omega_{cut} = 1.3\omega_{BM}$, as frequencies above are filtered out by the transmission line. However, we add two penalty terms that ensure that: a) the coefficients $[b_k]_{k=1..32}$ remain small; b) The function $\hat{\beta}(j\omega) = [1 - \sum_{k=1}^{32} b_k e^{-jk\omega\Delta t}]^{-1}$ has a small or negative imaginary part relative to its real part for frequencies above ω_{cut} .

The first condition is enforced by applying a penalty on the sum of squares of $[b_k]_{k=1..32}$, as in ridge regression. The second condition is controlled by penalizing $\max(0, \text{Im}(\hat{\beta})/\text{Re}(\hat{\beta}))$ above ω_{cut} , with the max operator applied element-wise. This penalty prevents situations where a monochromatic solution of the TL model, locally proportional to $\exp(-jk\omega\Delta t)$, becomes unstable at high frequencies due to a positive imaginary part in $\hat{\beta}$.

Appendix A. provides more details on the LSE regression used to determine the $[b_k]$ coefficients, including the full form of the cost function. We also describe a method that we used to enforce null gain of the correction factor at low frequencies, in Appendix B. . This precaution was taken to ensure that a low-frequency wave travels up to its peak as a planar wave (i.e., with a constant characteristic admittance)]Altoè and Shera (2020), since the opposite can lead to spurious behaviors (Shera and Zweig 1991).

The regression method presented above works for a given pair (ω_{BM}, G) . To achieve a continuous interpolation of the $[b_k]$ coefficients when (ω_{BM}, G) is allowed to vary, we applied a second regression method using a radial basis function neural network (RBF-NN). The input of the network is a tuple (ω_{BM}, G) and the output is the set of estimated coefficients $[b_k]_{k=1..32}$ that approximate β according to Eq. 13. The following

sentences provide more details on the RBF-NN and how it was trained. The inputs were first normalized to have input values between 0 and 1. There were 360 RBF centers (18×20), each associated with a Gaussian kernel of standard deviation 0.04. The kernel was made ‘local linear’ in the first dimension, meaning it was multiplied by an affine function with variable ω_{BM} . The RBF-NN was trained using stochastic gradient descent on randomly generated pairs (ω_{BM}, G) . Two strategies were considered for defining the cost function. In the first, targets $[b_k]$ are generated using the first method (penalized linear regression), and the Euclidean distance between the targets and the RBF-NN outputs is minimized. The second strategy directly minimizes the LSE cost function (on Eq. 14), bypassing the generation of $[b_k]$ coefficients from the first method. We trained the RBF-NN with 1,000 steps using the first strategy (learning rate: 0.1, momentum: 0.8) and 1,000 subsequent steps to fine-tune the parameters using the second strategy (learning rate: 1e-3, momentum: 0.9).

When simulating the traveling wave in response to a stimulus, generating the β coefficients on the fly using the RBF-NN can be computationally intensive. To reduce the computation time, we allowed the beta coefficients to be pre-computed and stored in a lookup table of size 1000×30 , where $N = 1000$ is the number of channels and 30 is the number of discrete steps covering the range of G values. The lookup table needs to be created only once, after which it can be reused for all simulations.

II.4.2 Integration of the new filters in the V-1D model

Note: in this subsection, we add the subscript n to the coefficients $[b_{n,k}]$ to emphasize the dependence of the filter coefficients on the TL section indexed by n .

The shunt admittance in the TL equations (Eq. 11) now includes the gain correction factor $\beta(j\omega)$ but the time-domain equations need to be updated accordingly. We introduce, as in Altoè et al. (2014), the variables:

$$g_n(t) = \omega_n^2 y_n(t) + \delta_n \omega_n v_n(t) - \varrho_n \omega_n^2 y_n(t - \tau_n),$$

$$q_n(t) = \frac{1}{L_{BM} M_{p_n}} p_n(t),$$

where $\tau_n = \psi_n / \omega_n$ and L_{BM} is the BM width. The law of motion including the pressure focusing factor gives:

$$\dot{q}_n = (\dot{v}_n + g_n) \cdot (1 - \sum_{k=1}^{32} b_{n,k} z^{-k}). \quad (15)$$

It is possible to separate current and past samples to get:

$$\begin{aligned} \dot{v}_n[t] &= q_n[t] - g_n[t] + Q_n[t], \text{ where} \\ Q_n[t] &= \sum_{k=1}^{32} b_{n,k} (\dot{v}_n[t - k\Delta t] + g_n[t - k\Delta t]). \end{aligned} \quad (16)$$

Equation 16 is very similar to the update equation in Diependaal et al. (1987) and Altoè et al. (2014), but with a dependence on past samples introduced through the new variable $Q_n(t)$. The second set of equations is derived from the relation between Δp and $\dot{v}_n(t)$ (Diependaal et al. 1987), which can be written as:

$$\mathbf{A}\mathbf{q} = \mathbf{g} - \mathbf{Q} \quad (17)$$

where \mathbf{A} is a tridiagonal matrix (see for example Eq. 2 in Verhulst et al. (2012)), and \mathbf{q} , \mathbf{g} , and \mathbf{Q} are the vector forms of $[q_n]$, $[g_n]$, and $[Q_n]$.

The simulation of BM motion follows the same approach as in Diependaal et al. (1987), by solving Eq. 17 then Eq. 16 at each step. To improve accuracy and efficiency, the V-1D model employs a RK4(5) adaptive numerical scheme (Altoè et al. 2014), which requires interpolating past values using cubic splines to account for the long-delay feedback term. We adopt the same strategy to provide an estimation of Q_n at each inner step. A complication is that Q_n contains a term depending on $\dot{v}_n[t - \Delta t] + g_n[t - \Delta t]$ (for $k = 1$), which cannot be interpolated using cubic splines because the value of $\dot{v}_n[t + \Delta t]$ is not yet known at timestep t . To address this, we split Q_n into two parts: the first term, $b_{n,1}(\dot{v}_n[t - \Delta t] + g_n[t - \Delta t])$, is estimated using Lagrange's quadratic interpolation with the points at $t - 2\Delta t$, $t - \Delta t$, and t . The second term, $\sum_{k=2}^{32} b_{n,k}(\dot{v}_n[t - k\Delta t] + g_n[t - k\Delta t])$, is interpolated with Catmull-Rom cubic splines using the same points and $t + \Delta t$.

II.4.3 Update of the filter coefficients during simulation

The correction gain factor β depends on the strength of the active process (variable G in the S-2D model) which varies over time as a function of response intensity. For each cochlear section, we compute a short-term average of intensity using a first-order recursive filter:

$$\langle I_n \rangle[t] = c_{n,0} v_n^2[t] + c_{n,1} v_n^2[t - \Delta t] - d_{n,1} \langle I_n \rangle[t - \Delta t]. \quad (18)$$

The coefficients $[c_n], [d_n]$ were chosen to implement a first-order low-pass Butterworth filter with a cut-off frequency of $f_n/2 = \omega_n/(4\pi)$. This cut-off ensures that the envelopes $\langle I_n \rangle(t)$ are smooth yet still react rapidly to changes in the signal intensity.

The V^* model retains the nonlinearities of the V-1D model that depend on the instantaneous velocity according to three different regimes: a linear regime up to a first transition point v_{knee1} , a compressive regime between v_{knee1} and a second transition point v_{knee2} , and a second linear regime above v_{knee2} . The trajectory of the BM admittance (double) pole value in the compressive regime is set by a constant compression slope, denoted as a , using a hyperbolic interpolation (Verhulst et al. 2018).

The V^* and V-1D model differ slightly in how the transition points are determined. The knee points are set using simulations of tone responses at the two linear regimes defined above. The poles are called the starting and saturating poles for the regime at low and high sound levels, respectively. For the gerbil model, we plotted the growth functions of v_{BM} at the CF=20 kHz place. Because the two regimes are linear, the growth functions are represented by straight lines when v_{BM} is plotted against the tone level (both values in dB). The growth function obtained with the starting poles is used to determine v_{knee1} , corresponding to I_{knee1_dB} , the sound level marking the onset of compression. The second transition point v_{knee2} is determined using the simulations with the saturating pole, by finding the intersection of the growth function with the line with equation $v_{dB} = v_{knee1_dB} + a(I_{dB} - I_{knee1_dB})$ where a is the compression slope. To calibrate the V^* model, we follow the same procedure, but the pressure focusing factor is set to its maximal value ($G = G_{\max}$) in the case of the starting pole, and to its minimal value ($G = G_{\min}$) in the case of the saturating pole. The calibration of compressive nonlinearities is illustrated at the end of the Results section.

Once the transition points are set, the pressure focusing factor, depending on G , can be updated dynamically. Within the compressive regime, G is determined by a linear interpolation between G_{\min} and G_{\max} with velocity values expressed in dB:

$$G(t) = G_{\max} + \frac{\langle I_n \rangle_{dB}(t) - 6 \text{ dB} - v_{knee1_dB}}{v_{knee2_dB} - v_{knee1_dB}} (G_{\min} - G_{\max}).$$

The -6 dB factor is an empirical factor to align $\langle I_n \rangle$ with the RMS values $v_{knee1,2}$. In the gerbil model simulations, the coefficients $[b_k]$ were updated according to this formula at every 6 timesteps (i.e., every 0.03 ms with $f_s = 200$ kHz).

III Results

III.1 Compressive response in the V-1D model

We begin by presenting the issue of insufficient compression in the initial V-1D model adapted to the gerbil physiology. Figure 3A shows the BM velocity growth for a tone stimulus. The simulations correctly feature a compressive regime flanked by two linear regimes at low and high stimulus levels. However, the range of sound levels over which compression occurs is limited to less than 30 dB. For the model version tailored to human hearing (Verhulst et al. 2018), the compressive regime spans 40 dB and presents a stronger compression slope. The origin of these distinct behaviors becomes clearer with the frequency responses shown in Fig. 3. These frequency responses were obtained by simulating BM responses to a slow linear chirp (2–10 kHz or 5–30 kHz), and analyzing the response with a sliding Gaussian window. In Fig. 3B, responses for the gerbil and human models are shown next to each other with comparable CFs (gerbil: 4 kHz, human: 5.5 kHz). It shows that the human model features a much sharper frequency tuning along with a broader range of response gain across sound levels. In the V-1D model, these two properties are coupled so that reducing the frequency selectivity results in less compression available.

Figure 3C confirms these observations at a higher CF and shows a comparison with published BM vibration data. In Fig. 3C and 3D we reproduced the frequency response measured in the basal turn of a live gerbil’s cochlea using optical coherence tomography (OCT) (He et al. 2022). The best frequency for the experimental data and the simulations is 19.5 kHz; for simplicity, we consider that $CF=20$ kHz throughout the text. The overlay with V-1D model simulations in Fig. 3C confirms similar frequency tuning, but the compression at the best frequency is weaker in the model by approximately 10 dB. The full range of compression can be restored in anW alternative model version with sharper tuning (Fig. 3D), but this comes at the cost of unrealistically high frequency selectivity at low sound levels. The trade-off between gain and frequency selectivity can shift the issue from insufficient compression to inadequate tuning, but the V-1D model cannot resolve both aspects simultaneously.

III.2 Short-wave gain compensation in the V^* model

The V^* model introduces partial gain compensation through the addition of a recursive all-pole filter (denoted by β), acting on top of the BM admittance. The magnitude and phase of β for different strengths of the active process are shown in Fig. 4. As expected, β has virtually no effect (gain of 0 dB) for low frequencies corresponding to the long-wave region, but exhibits stronger variations for short-wave frequencies (e.g., close to CF). The model only implements a version of the filter obtained through two successive regressions. The result of the second regression (RBF-NN) can deviate by 25% in magnitude from the initial target (S-2D model). The regression underestimates β if it represents a gain enhancement from the reference configuration, while it overestimates β in case of a gain reduction (i.e., $\beta < 1$). This indicates that the method is limited to relatively small corrections of the BM admittance. Nonetheless, the overall trend of β across frequencies and G values is well captured. The stability of the resulting filters was inspected by calculating numerically their poles and representing them in the z-domain. No case of instability was observed. The stability of the filters is promoted by the small filter coefficients that result from the ridge-like regression.

We simulated the responses to chirps at the $CF = 20$ kHz place for the V^* model as we did previously for the V-1D model. The results are shown in Fig. 5. The admittance correction did not alter the sharpness of the frequency response, but it extended the compression range by 5 dB. This outcome almost entirely reproduces the desired compression of the peak (seen as the maximum response shifting to lower frequencies with increasing sound levels). The compression of the response to a CF tone (20 kHz) remains slightly insufficient, falling short by 3 dBs. In addition, the compression achieved by the model is still associated with a broadening of the cochlear filters, while the quality factor in the experimental data is only reduced by half ($Q_{10dB} = 3.4$ at 20 dB vs. $Q_{10dB} = 1.7$ at 10 dB). As a result, the frequency responses are substantially broader at high sound levels compared to those observed experimentally.

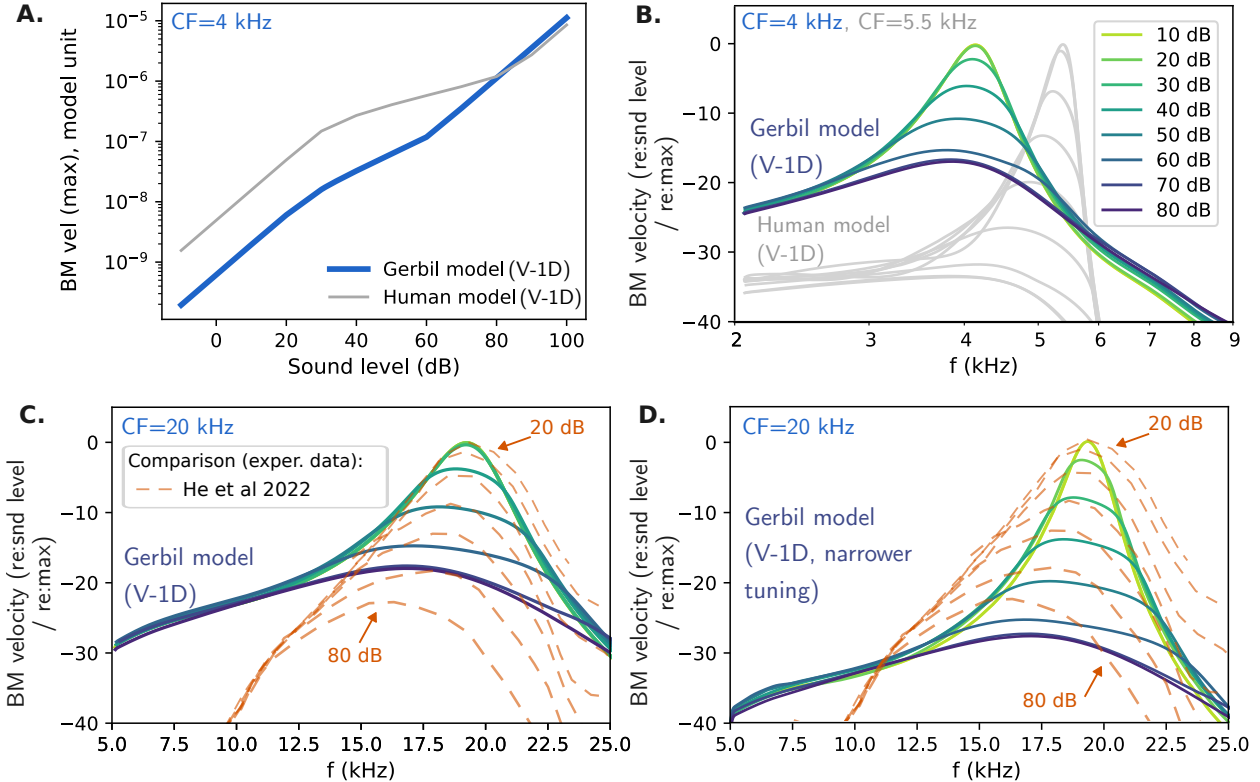


Figure 3: **Characteristic responses of the initial V-1D model.** **A.** BM velocity growth functions with respect to stimulus level at the place with $CF=4$ kHz (the stimulus is a CF tone). **B to D.** Frequency responses (magnitudes) of the V-1D model estimated by the BM velocity responses to a slow linear chirp presented at different sound levels. **B** Frequency response at the $CF= 4$ kHz place for the gerbil model (in color). Responses for the human model but at $CF=5.5$ kHz are also shown (in gray). **C.** Frequency response at the $CF=20$ kHz place. The color code for sound level is the same as in B. Vibration data from OCT measurements in gerbils (He et al. 2022) are overlayed with dashed lines. For the experimental data, sound levels are in dB SPL and velocity is relative to motion at the stapes. **D.** Same as C., but with a model version with sharper tuning. Figures B. to D.: ‘re: snd level / re: max’ indicates that the frequency responses were normalized to the the sound level and to the maximum peak magnitude of each curve set.

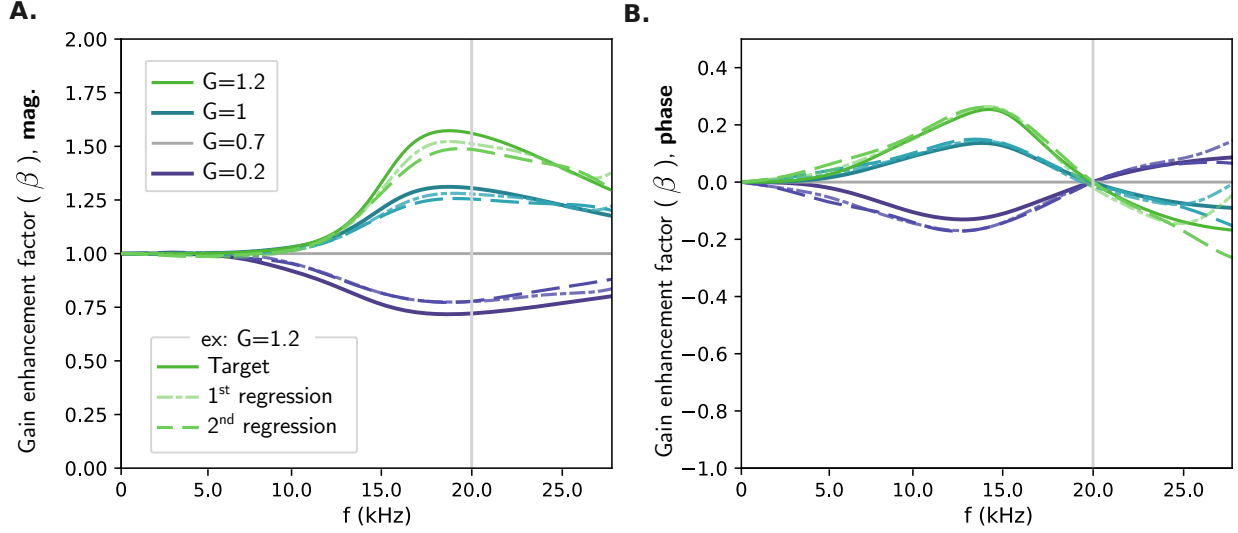


Figure 4: Gain enhancement factor β (**A.** gain and **B.** phase) for four different values of G (strength of the active process). The target was calculated using the recursive procedure described in Sisto et al. for the S-2D model and the relation $\beta = \alpha/\alpha_0$ where α_0 is the pressure focusing factor for $G_{REF} = 0.7$ (reference value). The dashed curves correspond to the regressions used to approximate β as a recursive all-pole filter. Dash-dotted: first regression (ridge regression). Dashed: second regression (RBF neural network). In the two panels, the vertical line corresponds to the BM characteristic frequency $\omega_{BM}/(2\pi)$.

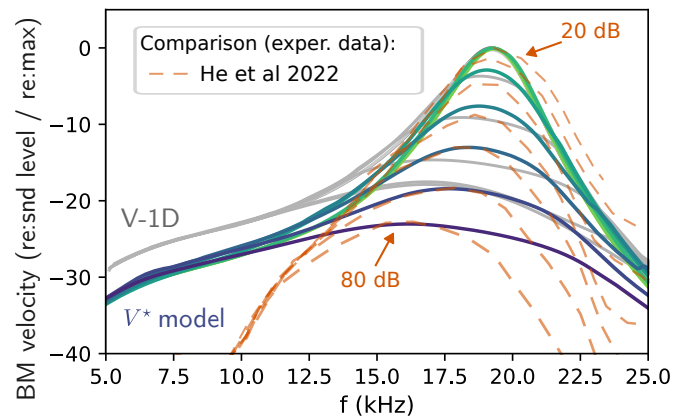


Figure 5: BM velocity magnitude normalized to sound level in response to tones for the V^* model (CF=20 kHz). The sound level goes from 20 to 80 dB in 10 dB steps (same color code as in Fig. 3). The responses for the V-1D model (gray lines) and real vibration data (dashed lines) are reproduced from Fig. 3.

III.3 Model calibration: update rate and compressive growth

Lastly, we present two additional figures related to the calibration of the V^* model. These figures address two key aspects of the model implementation: the temporal update of the gain compensation and the calibration of compressive nonlinearities.

The factor β in the V^* is updated over time based on a short-term average of output intensity $\langle I_n \rangle[t]$, which was defined in Methods II.4.3). To illustrate this temporal behavior, the response to a click at CF=20 kHz is shown in Fig.6A. The center panel also shows the time course of the intermediary variable G corresponding to the strength of the active process. G roughly follows the (vertically flipped) envelope of the BM response, as the active process is at its maximal strength at low intensity levels and inactive at high intensities. Fig.6A corresponds to the finer time sampling of G allowed by our model ($\Delta t = 5 \mu\text{s}$ or $f_s = 200 \text{ kHz}$). This sampling makes the simulations computationally intensive as the β filter coefficients are re-computed at each time step. With this sampling, the computation times were increased by a factor 20 compared to the V-1D model. To address this limitation, we tested other versions of the V^* model with slower update rates of the β filters. The corresponding impulse responses are shown in panels B and C of Fig.6. Differences with the faster update (panel A; baseline) are not easily seen on the time responses, but can be noticed on the frequency responses shown on the right. With an update rate of 0.06 ms (12 times slower than the fastest update), the magnitude was different from the baseline by up to $\sim 3 \text{ dB}$, which was considered too large. With an update rate of 0.03 ms (6 times slower), deviations were limited to $\sim 1 \text{ dB}$, which was considered as a good trade-off between computational efficiency and response consistency. The update rate of 0.03 ms was selected as the default one in our model. It reduces by almost a factor of 6 the computation time compared to the fastest update rate, but it still represents around 5 times the computation time of the V-1D model. However, by storing the filter coefficients in a lookup table —computed once at the first execution within a few seconds—the simulation times become comparable to those of the V-1D model. These computation times do not include data-saving operations, which in practice is the main bottleneck of the time-domain TL model, affecting both V-1D and V^* models.

The calibration of compressive nonlinearities, which was explained at the end of the Methods section, is illustrated with the gerbil model in Fig. 7A. The procedure is based on the response to a 20 kHz tone at the place with corresponding CF. The response is linear up to a first transition point, compressive up to a second transition point, and linear again at high sound levels. In the case of the V-1D model, the compressive regime is simply the transition between the two linear regimes, corresponding to a shift from a low-damped to a high-damped system. In the case of the V^* model, an additional factor of compression is the pressure focusing effect, which consists in a gain enhancement at the first transition point but gradually shifts to a gain reduction over the compressive regime. Figure 7 shows the response growth for the two models: panel A illustrates the growth functions expected from the calibration procedure, while panel B shows the actual responses obtained through simulations. The V^* model extends the compressive regime by 10 dB, which is more in line with the experimental data.

IV Discussion

IV.1 Improvement of compressive nonlinearities with the V^* model

We implemented a method to increase the range of response gain in the Verhulst et al. (V-1D) time-domain model, resulting in the modified V^* model. The proposed correction, based on autoregressive filters and regression methods, introduced an additional source of variation in gain in the frequency region corresponding to the short-wave region of the nonlinear traveling wave. The V^* model preserved most characteristics of the V-1D model while providing some decoupling between frequency selectivity and gain. This was illustrated in a gerbil model with simulations of BM velocity responses at the CF=20 kHz place. We showed that the compression of the peak response was increased by 5 dB (Fig.5) and the range of sound levels where compression occurs was extended by 10 dB (Fig.7). The limited range of cochlear response gain was already identified as a potential issue during the development of the V-1D model, which was originally designed based on human hearing (Verhulst et al. 2018). The issue appeared more prominent with recent efforts to adapt the model to small rodents, specifically gerbils and mice. The admittance correction proposed in

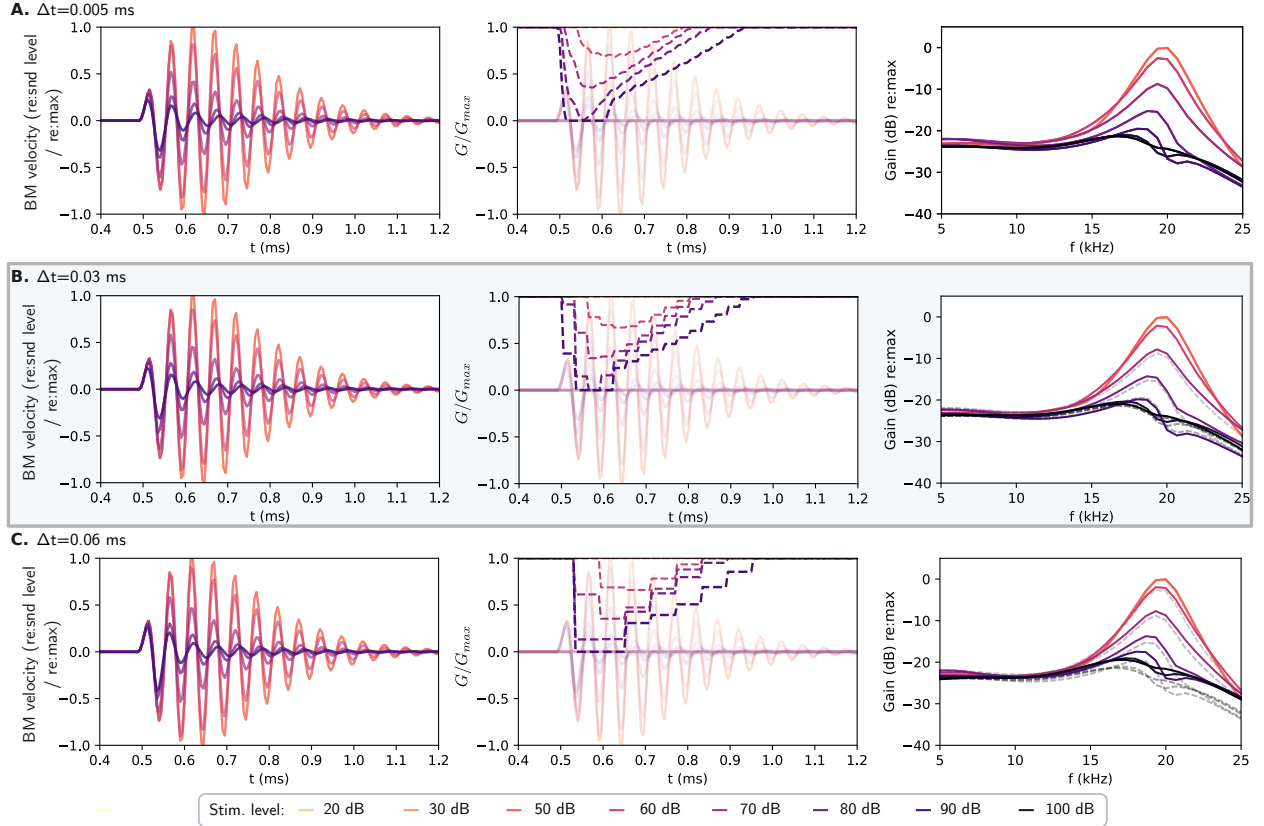


Figure 6: **Responses to clicks for the V^* model with different update rates.** **Left:** BM velocity responses in the time domain at the CF=20 kHz place, normalized with respect to the stimulus level. The responses are shown on a scale of [-1, 1] where 1 corresponds to the maximal BM response at the most sensitive state. The click was presented at 0.5 ms. **Center:** Time course of G/G_{max} (dashed curves) representing the strength of the active process used to compute the gain compensation factor. In the same figures, the traces of the click response have been represented (transparent curves). **Right:** Frequency responses corresponding to the left panel. The traces in the upper panel are reproduced in the panels below, in dashed gray, for comparison. Each row represents a different time resolution for the update of the gain correction: **A.** 0.005 ms, **B.** 0.03 ms **C.** 0.06 ms. The framed row ($\Delta t = 0.03$ ms) corresponds to the version used in the other figures of the Results section.

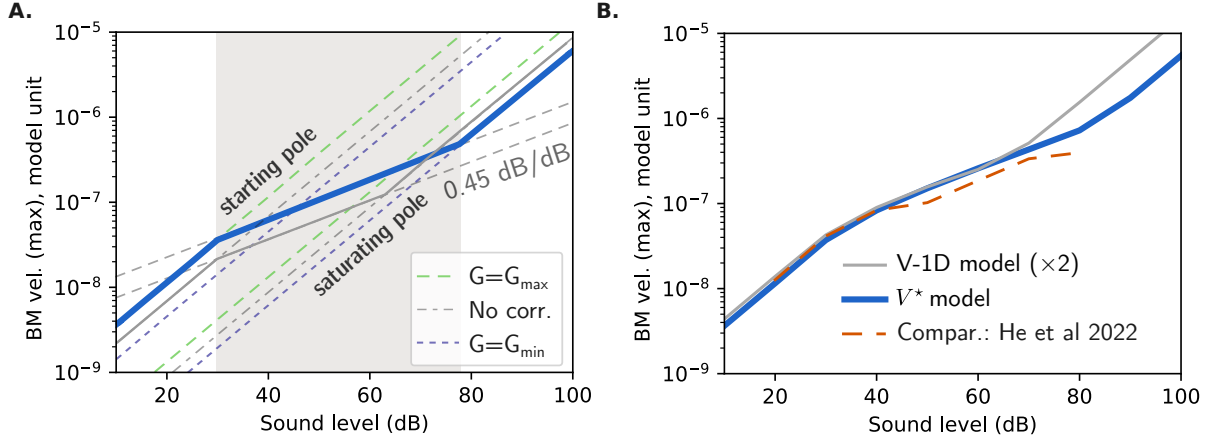


Figure 7: **Calibration of the BM compressive growth.** **A.** BM velocity growth functions simulated with different linear versions of the V^* model (dashed lines). The CF of the cochlear section is 20 kHz, and the stimulus probe is a 20 kHz tone. The responses are divided into two groups: ‘starting pole’ corresponds to a sharply tuned model, ‘saturating pole’ corresponds to a broadly tuned model adapted to high sound levels. Green lines were obtained with maximal gain enhancement ($G = G_{\max} = 1.3$) and dashed blue lines with maximal gain reduction ($G = G_{\min} = 0$). In addition, we show the theoretical growth function for the nonlinear V^* model as a solid thick blue line, and for the nonlinear V-1D model (no gain correction) as a solid gray line. The grayed area highlights the compressive regime. **B.** Actual growth functions obtained with the nonlinear V^* and V-1D models. The response for the V-1D model was vertically shifted (multiplied by a factor 2) to facilitate comparison. The growth function for the experimental data (He et al. 2022) is also shown (dashed curve).

this study offers a practical solution to compensate for limited compression in models for species with poor frequency selectivity, but could also be used to extend the compressive range for species with sharper tuning if deemed necessary.

However, the proposed method also presented some limitations in achieving a realistic response gain. As seen in the tip-to-tail ratio in Fig.5, the overall gain of the simulated filters is well below what is observed experimentally for the BM response. The 5 dB additional gain in the V^* model is not enough to significantly mitigate this issue. While our method captures the variations in peak gain with changes in sound level, the baseline gain — defined as the cochlear response gain in the passive state — is inherently limited by the time-domain implementation. This aspect is further discussed in the next subsection. This limitation explains why we used the β factor a target for the autoregressive filters, with maximal magnitude between 0.5 and 2 (Fig.4), instead of the pressure focusing factor α which can contribute approximately 20 dB of gain at the wave peak (Sisto et al. 2021). The β factor captures the variations in the α factor associated with changes in strength of the active process, instead of absolute gain. Thus, the V^* model is mostly relevant when considering a nonlinear model with variations of the cochlear response across sound levels. Even when considering only relative differences in gain, we showed that the regression and filter-design steps tended to reduce the size of the variations of the β factor (Fig.4).

Another concern regarding the V^* model is the difference in behavior between the base and apex of the cochlea. The targets for the β filters were calculated using the S-2D model, which assumes a constant cochlear height. In reality, the geometry of the cochlea is tapered, leading to a weaker pressure focusing factor (Eq. 4) at the apex than the base (Altoè and Shera 2020). Therefore, while in practice our method works for CFs below 20 kHz (e.g., we also analyzed the model response at 4 kHz), its connection to the physics of the cochlea becomes more questionable at the apex of the cochlea. In the core of the article, we validated our model against vibration data from the first turn of the gerbil cochlea (He et al. 2022), where experimental data are relatively abundant. Existing data measured at the cochlear apex (Meenderink et al. 2022) suggest that apical responses also exhibit large compression with limited changes in frequency

selectivity. It is not clear at this point whether the V^* model, if adjusted, could faithfully represent the physics of the cochlear apex.

IV.2 Difficulty of achieving high gain in a time-domain TL model

The previous paragraphs evoked the difficulty of achieving a high tip-to-tail ratio for a time-domain TL model reproducing wide-band BM responses. To understand why it remains a challenge for the V^* model, it is useful to consider a WKB approximation of a 1-D forward traveling wave in the form $v_{BM}(x, \omega) \propto Y_{BM}^{3/4}(x, \omega) \exp(-j \int_0^x \kappa(x', \omega) dx')$ (Reichenbach and Hudspeth 2014)². Factors contributing to the gain in v_{BM} can arise either directly from the admittance Y_{BM} , or from the exponential term. The limitations of admittance-based gain have already been mentioned throughout the article: they are tied to the trade-off between frequency selectivity and gain, well known in the case of a canonical bandpass filter. Here, we focus instead on how gain could be achieved through the second factor, the exponential term depending on the spatial integral of the complex wavelength.

In the sensitive cochlea, a monochromatic wave of pulsation ω is amplified in a small region basal to its peak, where the complex wavenumber $\kappa(x', \omega)$ has a positive phase. Assuming the property of scaling symmetry, this also implies that, at any given cochlear location x , $\kappa(x, \cdot)$ exhibits a positive phase in a narrow frequency range below the BM characteristic frequency (Altoè et al. 2021). Consequently, $\kappa(x, \cdot)$, when viewed as a filter, must include a region where the phase derivative is positive, corresponding to a negative group delay. This property carries over to the BM admittance. However, achieving negative group delay for causal filters is challenging; when it occurs, it results from phase interference between two wave packets that are necessarily delayed positively. In practice, a region of negative group delay is possible if it is compensated by a neighboring frequency region of larger magnitude with a positive group delay. As an illustration, the β filters for $G > 1$ in Fig.4 follow this pattern, with a negative group delay (positive phase derivative) below 14 kHz followed by a region of positive group delay (negative phase derivative) above 14 kHz associated with a larger response magnitude. The limitation described in this paragraph is accentuated by the fact that a causal filter with a large tip-to-tail ratio is typically associated with a large positive group delay in the tip region. Therefore, the two factors of BM velocity gain—either from the BM admittance or from wave propagation due to a region of negative resistance—cannot add up in the same frequency band.

It is therefore challenging to design causal filters that combine high tip-to-tail ratios with only modest positive phase shifts in the tip region. This severely limits the time implementation of a TL model, which relies exclusively on causal components. However, this raises the question: how does this argument differ for the actual cochlea? This question is relevant because causality constraints also apply to physical systems (i.e., Kramers-Kronig relations (Shera 2007)), yet the v_{BM} data exhibit a high tip-to-tail ratio. In reality, causality constraints in the case of the cochlear traveling wave are not as strict as they may seem initially, because global wave causality should be considered along with local ‘point-causality,’ with the former being more flexible than the latter. Local ‘point-causality’ refers to causal relations between local variables, while global wave causality also accounts for wave effects that can propagate up to the speed of the wavefront, appearing quasi-instantaneous to a local observer. For the time implementation, we have framed the factors α or β as part of the updated BM admittance. However, a more accurate physical interpretation would treat these factors as distinct from the local BM admittance. Instead, the pressure focusing factor α is associated with the forward pressure wave which separates the frequency components as they travel along the cochlea. The dispersive nature of the wave means that each wave component is affected differently by pressure focusing, independently of the delays imposed by the local BM mechanical response. Consequently, translated as a filter, α is not required to be causal, i.e., the translation of local ‘point-causality’, although it must respect global wave causality. Free of that constraint, it can significantly and almost instantaneously enhance the frequency response associated with the short-wave components, achieving up to +20 dB gain with very short group delays. This subtle but important distinction highlights the challenge of adapting a 2-D frequency-domain model into a 1-D time-domain model, a complexity not immediately apparent from the equations, as it emerges from a non-trivial interpretation of causality.

²This formula is valid for a box model where the fluid impedance $Z_f = \frac{2j\omega\rho}{H}$ is considered constant. For a tapered-box model in the long-wave approximation, as in Zweig 1991 (hence, as in the V-1D model), the normalization factor also includes $1/\sqrt{H}$, which is ignored here as it depends on position but not on ω .

The assumption of local causality can even be questioned for the BM admittance Y_{BM} , at least when it accounts for the BM mechanical response within the framework of the traveling wave, rather than treating the BM as an isolated segment. This point is well illustrated by the S-2D model, in which Y_{BM} includes a viscous damping term that depends on the wave profile and is influenced by the dispersive nature of the wave. More specifically, the viscous stress in the admittance is related to the second spatial derivative of the pressure field. When expressed in terms of v_{BM} , it again introduces the factor α (Eq.6), proportional to k in the short-wave region. A wavelength-dependent admittance is present in other models: for instance, it is found in the recent work of Elliott et al. which includes longitudinal coupling via a viscoelastic model of the tectorial membrane (Elliott et al. 2024). An admittance model that relaxes the local point-causality constraint can remove oscillations in the admittance phase seen in time-domain implementations (at frequencies below CF) (Shera 2001), allowing for an extended region of negative resistance in the frequency and spatial domains.

Because of the difficulty of simulating a region of negative resistance with a causal and stable model, it appears necessary for a time-domain implementation to exploit the resonance of the BM admittance in order to generate a tall response peak. For time-domain models, it is then highly expected that the wave in response to a CF tone peaks at the cochlear place where the characteristic frequency is equal to CF, i.e., where the stiffness and mass terms in the admittance cancel each other. This is especially true for the V-1D model, as already mentioned in the Methods section II.3. Although this property appears natural, almost tautological, it is not necessarily a feature of a 2-D frequency model (it is not in the S-2D model). If the wavenumber increases sharply in a region basal to the characteristic place, there can be enough gain (through α) and increase in damping (through viscous damping) so that a tall peak followed by a steep roll-off are generated in the stiffness-dominated region of the cochlea before the wave reaches the CF place (Sisto et al. 2021; Deloche et al. 2025; Sisto and Moleti 2024). The occurrence of the traveling-wave peak in the stiffness-dominated region appears more consistent with simultaneous measurements of pressure and BM displacement in the cochlea (Dong and Olson 2013), although this question remains a topic of debate.

IV.3 Two types of nonlinearities in the V^* model

The V^* model achieves compression through two different implementation strategies. In the final comments of this paper, we reflect on these differences and on how this dual approach may prove useful in other contexts.

The solution with the gain enhancement factor β differs from the initial BM admittance model as it relies on numerical methods rather than an analytical derivation. The initial V-1D admittance model is based on a reduced number of parameters (Eq.11) which have a direct interpretation in terms of stiffness-to-weight ratio, damping, magnitude or delay of the slow feedback term. Except for the slow feedback term, the impedance terms involve time derivatives (up to second order), corresponding to (quasi-)instantaneous local dynamics. By contrast, the recursive β filters include a weighted sum of the previous 32 past values, allowing for slower dynamics. The resulting filter has a smoother, less stereotyped frequency response than the analytical form, but can be adjusted to match a desired broadband shape with more flexibility. We used as target the pressure focusing factor computed from the S-2D model, but filter shapes from other models could be used as well. The important point is that the methods presented here are designed to adjust the admittance rather than to reproduce its characteristic form, which in the V-1D model results from a carefully controlled resonance. The V-1D admittance equations therefore remain the core of the V^* TL model. These equations are constrained by the main poles' trajectory, set to maintain the near-invariance of BM velocity zero crossings (Shera 2001). A potential way to generate more compression at CF would be to lower the local resonant frequency of the BM admittance as sound level increases. This would accentuate the basal shift of the wave peak and result in a larger decrease of the response gain to a CF tone with increasing sound levels. However, this approach would also alter the admittance phase response and disrupt the near-invariance of zero-crossings. A different way to include pressure focusing in a 1-D model is to integrate the contributions of pressure sources along the cochlear partition using the Green-function formalism (Diependaal and Viergever; Duifhuis 2012; Ver Hulst), but this approach is computationally very demanding.

Lastly, the two implementations of compressive nonlinearity differ as they instantiate different types of nonlinear dynamics. Like the V-1D model, the V^* model is primarily driven by instantaneous nonlinearities, assumed to enhance cochlear motion on a cycle-by-cycle basis (Dewey et al. 2021). But the gain enhancement

factor β , based on a feedback loop, also introduces non-instantaneous nonlinearities. The strength of pressure focusing follows a vertically-flipped envelope of BM velocity (Fig. 6). Practically, this choice speeds up computation since the filter coefficients do not need to be updated at every timestep. But this choice is also motivated by a physical argument: a change in the wavenumber cannot be instantaneous and necessarily requires integration over a time window. Although most cochlear models include instantaneous nonlinearities, there has been some debate on whether the active process could instead follow a feedback loop based on the signal envelope, akin to an automatic gain control (AGC) scheme (Van Der Heijden 2005; Cooper and van der Heijden 2016; Altoè et al. 2017). In our model, a part of the nonlinearities are driven by a feedback loop, but these originally arise from a passive phenomenon (pressure focusing) that accompanies changes in the active process. As a result, the mechanisms underlying the nonlinear compressive response are still considered instantaneous in the case of the V^* model. Regardless of its passive or active origin, the type of nonlinear dynamics in the cochlea has significant implications. For example, instantaneous nonlinearities or envelope-based control loops produce distortion products with different effect sizes (Duifhuis 2012) or phase properties (Van Der Heijden 2005). In this regard, the V^* model or a variant, with its ability to simulate complex hybrid dynamics, could prove useful for investigating advanced temporal aspects of cochlear mechanics.

In conclusion, we presented a method to implement an additional factor of variation of gain response in a 1-D TL model. The factor partly reproduced the response ‘boost’ observed in the short-wave region in 2-D models. The resulting V^* model generated 5 dB more gain (or compression) at the wave peak. This method proved useful for developing TL models tailored to the physiology of small mammals, specifically rodents. Developing such models is valuable as part of a translational approach, as common laboratory animals provide extensive insights about normal and impaired hearing. However, achieving this correction required a sophisticated approach involving regression and filter-design methods. Overall, this work highlights the challenge of translating wavelength-dependent phenomena into a time-domain TL implementation while maintaining computational efficiency.

Acknowledgments

This project was funded by the FWO project “Audimod” G068621N and ERA-NET project “CoSySpeech” (G0H6420N).

Appendices

A. Full form of the cost function for the LSE regression

The first regression leads to the estimation of coefficients $[b_k]_{k=1..32}$ for a given pair (ω_{BM}, G) . For this step, we use a regular discretization of frequencies $(0, f_s/(2m_2), \dots, m_1 f_s/(2m_2), \dots, (m_2 - 1) f_s/(2m_2))$ covering the interval $[0, f_s/2]$ where $f_s/2$ is the Nyquist frequency for the TL simulations. In our case, $f_s = 200$ kHz and $m_2 = 512$. The set of discrete frequencies is further divided into $(0, \dots, (m_1 - 1) f_s/(2m_2))$ and $(m_1 f_s/(2m_2), \dots, (m_2 - 1) f_s/(2m_2))$ which correspond to the frequencies below and above $\omega_{cut} = 1.3 \omega_{BM}$.

We define the following ‘feature’ matrices:

$$X_{l,re} = [\cos(\pi(km)/m_2)]_{m=0..m_1-1, k=1..32}, \quad (19a)$$

$$X_{l,im} = -[\sin(\pi(km)/m_2)]_{m=0..m_1-1, k=1..32}, \quad (19b)$$

$$X_{r,re} = [\cos(\pi(km)/m_2)]_{m=m_1..m_2-1, k=1..32}, \quad (19c)$$

$$X_{r,im} = -[\sin(\pi(km)/m_2)]_{m=m_1..m_2-1, k=1..32}. \quad (19d)$$

l stands for ‘left’, r stands for ‘right’. Following Eq. 13, we have

$$Y_{l,re} = \operatorname{Re}(1 - 1/\beta) \approx 1 - \operatorname{Re}(1/\hat{\beta}) = X_{l,re}b, \quad (20a)$$

$$Y_{l,im} = \operatorname{Im}(1 - 1/\beta) \approx -\operatorname{Im}(1/\hat{\beta}) = X_{l,im}b, \quad (20b)$$

where b is the vector of the coefficients (b_k) .

The full LSE cost function is then:

$$LSE(b) = \|Y_{l,re} - X_{l,re}b\|_2^2 + \|Y_{l,im} - X_{l,im}b\|_2^2 + \lambda_1 \|b\|_2^2 + \lambda_2 \left\| \max(0, \frac{X_{r,Im}b}{1 - X_{r,Re}b}) \right\|_2^2 \quad (21)$$

where $\|\cdot\|_2$ is the Euclidian norm. The cost function includes two penalties, weighted by λ_1 and λ_2 , that prevent large coefficients b_k and large positive phase values in $\hat{\beta}$ for frequencies above ω_{cut} . In the second penalty, $\frac{X_{r,Im}b}{1 - X_{r,Re}b}$ corresponds to $\operatorname{Im}(\hat{\beta})/\operatorname{Re}(\hat{\beta})$, expressed with the feature matrices and with the division applied element-wise.

The LSE cost function (Eq. 21) was minimized using the function `leastsq` of `scipy`, which is based on the Levenberg-Marquardt (LM) algorithm.

B. Enforcing null gain of the correction factor for low frequencies

One caveat of the method described above (i.e., using Eq. 21) is that the estimated filter $\hat{\beta}(\omega)$ is not guaranteed to be of magnitude 1 when $\omega \rightarrow 0$. One option to enforce $\beta(0) = (1 - \sum_{k=1}^{32} b_k)^{-1} = 1$ would be to constrain the coefficients $[b_k]$ to the hyperplane $\sum_{k=1}^{32} b_k = 0$, but we found that this solution was too rigid, resulting in undesired behaviors.

Instead, we included a gain factor $K = 1 + \epsilon$ in the regression used to determine the filter coefficients, which was adjusted after optimization to enforce a null gain (in dB) at frequency 0. Specifically, Eq. 13 is replaced with:

$$\beta(z^{-1}) \approx \frac{1 + \epsilon}{1 - \sum_{k=1}^{32} b_k z^{-k}}. \quad (22)$$

This updates Eq. 20 to:

$$\operatorname{Re}(1 - 1/\beta) - \epsilon \operatorname{Re}(1/\beta) \approx X_{l,re}b, \quad (23a)$$

$$\operatorname{Im}(1 - 1/\beta) - \epsilon \operatorname{Im}(1/\beta) \approx X_{l,im}b, \quad (23b)$$

which leads to the modified LSE function:

$$LSE(b, \epsilon) = \|Y_{l,re} - X_{l,re}b + (Y_{l,re} - 1)\epsilon\|_2^2 + \|Y_{l,im} - X_{l,im}b + Y_{l,im}\epsilon\|_2^2 + \lambda_1 (\|b\|_2^2 + \epsilon^2) + \lambda_2 \left\| \max(0, \frac{X_{r,Im}b}{1 - X_{r,Re}b}) \right\|_2^2. \quad (24)$$

The extended LSE cost was minimized as before using a LM algorithm, with ϵ as a regressor in addition to the $[b_k]$ coefficients. After the optimization was done, we set the desired gain of the transfer function $K = 1 + \epsilon$ by updating ϵ following $\epsilon \leftarrow -\sum_{k=1}^{32} b_k$.

References

Alessandro Altoè and Christopher A. Shera. The cochlear ear horn: Geometric origin of tonotopic variations in auditory signal processing. *Scientific Reports*, 10:20528, November 2020. ISSN 2045-2322. doi: 10.1038/s41598-020-77042-w.

Alessandro Altoè, Ville Pulkki, and Sarah Verhulst. Transmission line cochlear models: Improved accuracy and efficiency. *The Journal of the Acoustical Society of America*, 136(4):EL302–EL308, September 2014. ISSN 0001-4966. doi: 10.1121/1.4896416.

Alessandro Altoè, Karolina K. Charaziak, and Christopher A. Shera. Dynamics of cochlear nonlinearity: Automatic gain control or instantaneous damping? *The Journal of the Acoustical Society of America*, 142(6):3510–3519, December 2017. ISSN 0001-4966, 1520-8524. doi: 10.1121/1.5014039.

Alessandro Altoè, Karolina K. Charaziak, James B. Dewey, Arturo Moleti, Renata Sisto, John S. Oghalai, and Christopher A. Shera. The Elusive Cochlear Filter: Wave Origin of Cochlear Cross-Frequency Masking. *Journal of the Association for Research in Otolaryngology* 2021, pages 1–18, October 2021. ISSN 1438-7573. doi: 10.1007/S10162-021-00814-2.

Deepak Baby, Arthur Van Den Broucke, and Sarah Verhulst. A convolutional neural-network model of human cochlear mechanics and filter tuning for real-time applications. *Nature machine intelligence*, 3(2):134–143, February 2021. ISSN 2522-5839. doi: 10.1038/s42256-020-00286-8.

Karolina K. Charaziak and Christopher A. Shera. Reflection-Source Emissions Evoked with Clicks and Frequency Sweeps: Comparisons Across Levels. *JARO: Journal of the Association for Research in Otolaryngology*, 22(6):641–658, December 2021. ISSN 1525-3961. doi: 10.1007/s10162-021-00813-3.

Nigel P. Cooper and Marcel van der Heijden. Dynamics of cochlear nonlinearity. In Pim van Dijk, Deniz Baskent, Etienne Gaudrain, Emile de Kleine, Andreas Wagner, and Casper Lanting, editors, *Physiology, Psychoacoustics and Cognition in Normal and Impaired Hearing*, pages 267–273. Springer, Berlin, 2016.

François Deloche, Morgan Thienpont, Arturo Moleti, Renata Sisto, and Sarah Verhulst. Active control of transverse viscoelastic damping in the tectorial membrane: A second mechanism for traveling-wave amplification? *Hearing Research*, 464:109320, 2025. ISSN 03785955. doi: 10.1016/j.heares.2025.109320.

James B. Dewey, Alessandro Altoè, Christopher A. Shera, Brian E. Applegate, and John S. Oghalai. Cochlear outer hair cell electromotility enhances organ of Corti motion on a cycle-by-cycle basis at high frequencies in vivo. *Proceedings of the National Academy of Sciences*, 118(43):e2025206118, October 2021. doi: 10.1073/pnas.2025206118.

Rob J. Diependaal and Max A. Viergever. Nonlinear and active two-dimensional cochlear models: Time-domain solution. 85(2):803–812. ISSN 0001-4966. doi: 10.1121/1.397553. URL <https://doi.org/10.1121/1.397553>.

Rob J. Diependaal, H. Duifhuis, H. W. Hoogstraten, and Max A. Viergever. Numerical methods for solving one-dimensional cochlear models in the time domain. *The Journal of the Acoustical Society of America*, 82(5):1655–1666, November 1987. ISSN 0001-4966, 1520-8524. doi: 10.1121/1.395157.

Wei Dong and Elizabeth S. Olson. Detection of Cochlear Amplification and Its Activation. *Biophysical Journal*, 105(4):1067–1078, August 2013. ISSN 0006-3495. doi: 10.1016/j.bpj.2013.06.049.

Hendrikus Duifhuis. *Cochlear Mechanics: Introduction to a Time Domain Analysis of the Nonlinear Cochlea*. Springer US, Boston, MA, 2012. ISBN 978-1-4419-6116-7 978-1-4419-6117-4. doi: 10.1007/978-1-4419-6117-4.

Stephen Elliott, Riccardo Marrocchio, and Karl Grosh. Forms of longitudinal coupling in the organ of Corti. *AIP Conference Proceedings*, 3062(1):020014, February 2024. ISSN 0094-243X. doi: 10.1063/5.0189306.

Elika Fallah, C. Elliott Strimbu, and Elizabeth S. Olson. Nonlinearity of intracochlear motion and local cochlear microphonic: Comparison between guinea pig and gerbil. *Hearing Research*, 405:108234, June 2021. ISSN 03785955. doi: 10.1016/j.heares.2021.108234.

Wenxuan He, George Burwood, Edward V. Porsov, Anders Fridberger, Alfred L. Nuttall, and Tianying Ren. The reticular lamina and basilar membrane vibrations in the transverse direction in the basal turn of the living gerbil cochlea. *Scientific Reports*, 12(1):19810, November 2022. ISSN 2045-2322. doi: 10.1038/s41598-022-24394-0.

Sebastiaan W. F. Meenderink, Xiaohui Lin, B. Hyle Park, and Wei Dong. Sound Induced Vibrations Deform the Organ of Corti Complex in the Low-Frequency Apical Region of the Gerbil Cochlea for Normal Hearing : Sound Induced Vibrations Deform the Organ of Corti Complex. *Journal of the Association for Research in Otolaryngology: JARO*, 23(5):579–591, October 2022. ISSN 1438-7573. doi: 10.1007/s10162-022-00856-0.

Marcus Müller. The cochlear place-frequency map of the adult and developing mongolian gerbil. *Hearing Research*, 94(1):148–156, May 1996. ISSN 0378-5955. doi: 10.1016/0378-5955(95)00230-8.

T. Reichenbach and A. J. Hudspeth. The physics of hearing: Fluid mechanics and the active process of the inner ear. *Reports on Progress in Physics*, 77(7):076601, July 2014. ISSN 0034-4885, 1361-6633. doi: 10.1088/0034-4885/77/7/076601.

Mario A. Ruggero, Nola C. Rich, Alberto Recio, S. Shyamla Narayan, and Luis Robles. Basilar-membrane responses to tones at the base of the chinchilla cochlea. *The Journal of the Acoustical Society of America*, 101(4):2151–2163, April 1997. ISSN 0001-4966. doi: 10.1121/1.418265.

Amin Saremi, Rainer Beutelmann, Mathias Dietz, Go Ashida, Jutta Kretzberg, and Sarah Verhulst. A comparative study of seven human cochlear filter models. *The Journal of the Acoustical Society of America*, 140(3):1618–1634, September 2016. ISSN 0001-4966. doi: 10.1121/1.4960486.

Christopher A. Shera. Intensity-invariance of fine time structure in basilar-membrane click responses: Implications for cochlear mechanics. *The Journal of the Acoustical Society of America*, 110(1):332–348, July 2001. ISSN 0001-4966. doi: 10.1121/1.1378349.

Christopher A. Shera. Laser amplification with a twist: Traveling-wave propagation and gain functions from throughout the cochlea. *The Journal of the Acoustical Society of America*, 122(5):2738–2758, November 2007. ISSN 0001-4966, 1520-8524. doi: 10.1121/1.2783205.

Christopher A Shera and Karolina K Charaziak. Cochlear frequency tuning and otoacoustic emissions. *Cold Spring Harbor Perspectives in Medicine*, 9(2), 2019. ISSN 21571422. doi: 10.1101/cshperspect.a033498.

Christopher A. Shera and George Zweig. A symmetry suppresses the cochlear catastrophe. *The Journal of the Acoustical Society of America*, 89(3):1276–1289, March 1991. ISSN 0001-4966, 1520-8524. doi: 10.1121/1.400650.

Christopher A Shera, John J Guinan, and Andrew J Oxenham. Revised estimates of human cochlear tuning from otoacoustic and behavioral measurements. 99(5):3318–3323. ISSN 0027-8424. doi: 10.1073/pnas.032 675099. URL <http://www.ncbi.nlm.nih.gov/pubmed/11867706>.

Renata Sisto and Arturo Moleti. The tonotopic cochlea puzzle: A resonant transmission line with a “non-resonant” response peak. *JASA Express Letters*, 4(7):074401, 2024. ISSN 2691-1191. doi: 10.1121/10.002 8020.

Renata Sisto, Daniele Belardinelli, and Arturo Moleti. Fluid focusing and viscosity allow high gain and stability of the cochlear response. *The Journal of the Acoustical Society of America*, 150(6):4283–4296, December 2021. ISSN 0001-4966. doi: 10.1121/10.0008940.

Renata Sisto, Daniele Belardinelli, Alessandro Altoè, Christopher A. Shera, and Arturo Moleti. Crucial 3-D viscous hydrodynamic contributions to the theoretical modeling of the cochlear response. *The Journal of the Acoustical Society of America*, 153(1):77–86, January 2023. ISSN 0001-4966. doi: 10.1121/10.0016809.

Morgan Thienpont, Francois Deloche, Sarineh Keshishzadeh, Danill Kiselev, Jérôme Bourien, Jean-Luc Puel, Brad Buran, Naomi Bramhall, and Sarah Verhulst. Translating a Computational Model of the Human Auditory Periphery to Gerbil and Mouse for Comparative Auditory Research. In *Mechanics of Hearing Workshop 2024 (MoH 24)*, Ann Arbor, USA, June 2024. Zenodo. doi: 10.5281/zenodo.13769392.

Marcel Van Der Heijden. Cochlear gain control. *The Journal of the Acoustical Society of America*, 117(3): 1223–1233, March 2005. ISSN 0001-4966, 1520-8524. doi: 10.1121/1.1856375.

Alejandro Osses Vecchi, Léo Varnet, Laurel H. Carney, Torsten Dau, Ian C. Bruce, Sarah Verhulst, and Piotr Majdak. A comparative study of eight human auditory models of monaural processing. *Acta Acustica*, 6: 17, 2022. ISSN 2681-4617. doi: 10.1051/aacus/2022008.

Henri Ver Hulst. Marrying the physics of critical oscillators with traveling-wave models of the cochlea.

Sarah Verhulst, Torsten Dau, and Christopher A. Shera. Nonlinear time-domain cochlear model for transient stimulation and human otoacoustic emission. *The Journal of the Acoustical Society of America*, 132(6): 3842–3848, December 2012. ISSN 0001-4966. doi: 10.1121/1.4763989.

Sarah Verhulst, Hari M. Bharadwaj, Golbarg Mehraei, Christopher A. Shera, and Barbara G. Shinn-Cunningham. Functional modeling of the human auditory brainstem response to broadband stimulation. *The Journal of the Acoustical Society of America*, 138(3):1637–1659, September 2015. ISSN 0001-4966. doi: 10.1121/1.4928305.

Sarah Verhulst, Alessandro Altoè, and Viacheslav Vasilkov. Computational modeling of the human auditory periphery: Auditory-nerve responses, evoked potentials and hearing loss. *Hearing Research*, 360:55–75, March 2018. ISSN 0378-5955. doi: 10.1016/j.heares.2017.12.018.

Eric Verschooten, Christian Desloovere, and Philip X. Joris. High-resolution frequency tuning but not temporal coding in the human cochlea. *PLOS Biology*, 16(10):e2005164, October 2018. ISSN 1545-7885. doi: 10.1371/journal.pbio.2005164.

G. Zweig. Finding the impedance of the organ of Corti. *The Journal of the Acoustical Society of America*, 89(3):1229–1254, March 1991. ISSN 0001-4966. doi: 10.1121/1.400653.